Research article

Evaluation of SnO$_2$ for sunlight photocatalytic decontamination of water

M. Aslam [a], M. Tariq Qamar [b], Shahid Ali [c], Ateeq Ur Rehman [d], M.T. Soomro [a], Ikram Ahmed [e], I.M.I. Ismail [a, f], A. Hameed [a, g, *]

[a] Center of Excellence in Environmental Studies, King Abdulaziz University, Jeddah 21589, Saudi Arabia
[b] Department of Chemistry, Forman Christian College (A Chartered University), Ferozepur Road, Lahore, 54600, Pakistan
[c] Center of Excellence in Nanotechnology, King Fahd University of Petroleum & Minerals, Dhahran 31261, Saudi Arabia
[d] School of Chemical Engineering, The University of Queensland, St Lucia, QLD, 4067, Australia
[e] Department of Applied Chemistry, Government College University, Faisalabad 38000, Pakistan
[f] Chemistry Department, Faculty of Science, King Abdulaziz University, Jeddah 21589, Saudi Arabia
[g] National Center of Physics, Quaid-e-Azam University, Islamabad 44000, Pakistan

ARTICLE INFO

ABSTRACT

The broad bandgap tin (IV) oxide (SnO$_2$) is the least investigated semiconductor material for photocatalytic water decontamination in sunlight exposure. A detailed study covering the synthesis, characterization and the evaluation of photocatalytic activity of SnO$_2$, in the natural sunlight exposure, is presented. The structural characterization by XRD revealed the formation of phase pure tetragonal SnO$_2$ with the average crystallite size of ~41.5 nm whereas minor Sn^{2+} states in the material were identified by XPS analysis. As explored by diffuse reflectance (DR) and photoluminescence (PL) spectroscopy, the material exhibited a distinct absorption edge at ~3.4 eV. The morphological and microstructure analysis of the synthesized SnO$_2$ was carried out by FESEM and HRTEM. The electrochemical impedance spectroscopy (EIS) and chronopotentiometry (CP) predicted the better charge transport and retention ability of the material under illumination whereas the Mott-Schottky extrapolation prophesied the n-type behavior with the flat-band potential of −0.60 V. The photocatalytic activity of SnO$_2$ was assessed in the exposure of complete spectrum natural sunlight for the removal of 2,4,6-trichlorophenol. The HPLC and TOC analysis monitored the progress of degradation and mineralization whereas the released chloride ions were evaluated by ion chromatography. The effect of the transition metal ions (Fe^{3+}, Cu^{2+}, Ni^{2+} and Zn^{2+}) as electron capture agents and H$_2$O$_2$ as ROS generator was explored during the degradation process. The utility of the material for the simultaneous removal of chlorophenols in the mixture was also investigated. The SnO$_2$ exhibited sustained activity in the repeated use. Based on experimental evidence congregated, the mechanism of the removal process and the efficacy of SnO$_2$ for sunlight photocatalytic decontamination of water was established.

© 2018 Elsevier Ltd. All rights reserved.

1. Introduction

The natural sunlight assisted wastewater decontamination, because of abundance, ever renewability and cost effectiveness is a perspective and rapidly growing area of research for the photocatalytic removal of hazardous toxins from the polluted water (Chou et al., 2016). The metal oxide semiconductors, due to chemical stability and non-toxic nature are the extensively promised surfaces for the generation of reactive oxygen species (ROS) with the absorption of sunlight photons (Affam and Chaudhuri, 2013; Aslam et al., 2015a; Khaki et al., 2017; Qamar et al., 2015; Salah et al., 2016). Although, several semiconducting metal oxides that includes TiO$_2$, ZnO, WO$_3$, Bi$_2$O$_3$, CeO$_2$ etc. have been extensively investigated for the photocatalytic treatment of environmental pollutants (Aslam et al., 2014a, 2016; Hameed et al., 2015; Linsebigler et al., 1995; Nakata and Fujishima, 2012; Ollis and Al-Ekabi, 1993; Schneider et al., 2014; Yin et al., 2009; Zhang et al.,

2010; Zhong et al., 2014). However, the efforts to explore the impending contestants among the metal oxides for the effective removal of toxicants from the wastewater are still in progress (Dai et al., 2012). Among the semiconductor oxides, SnO_2, due to the comparable optical-electrical and chemical properties, is a least-investigated potential contender in this regard (Diallo et al., 2016; Dimitrov et al., 2010). SnO_2, an *n-type* semiconductor with a wide bandgap has proved its worth in a variety of commercial applications (Das and Jayaraman, 2014; Zhao et al., 2014; Zhou et al., 2014). Although, few reports regarding the photocatalytic activity of SnO_2 for the removal of dyes/phenol are available in the literature (Al-Hamdi et al., 2015; Mendoza-Damián et al., 2015; Singh et al., 2014; Wang et al., 2013; Yao et al., 2014), however, the comprehensive depiction of the photocatalytic behavior of SnO_2 in sunlight exposure, the nature of ROS generated and the efficiency to remove potential pollutants such as chlorophenol derivatives lack. Among the chloro-substituted phenols, 2,4,6-trichlorophenol (TCP), due to stable and non-biodegradable chemical structure, is the substrate of interest in water decontamination (Ghanbari et al., 2016; Peng et al., 2015; Qamar et al., 2016; Xu and Wang, 2015). The pure phase, doped, and composite materials of both TiO_2 and ZnO have been investigated for the photocatalytic removal of TCP (Abbas et al., 2016; Carevic et al., 2016; Gaya et al., 2010; Ji et al., 2013; Rengaraj and Li, 2006; Sood et al., 2015; Sun and Xu, 2009; Wang et al., 2012; Xiong et al., 2005; Yang et al., 2016).

The current study is a detailed evaluation of the photocatalytic activity of surfactant-assisted hydrothermally synthesized SnO_2 in natural sunlight exposure for the photocatalytic decontamination of water. Prior to the photocatalytic studies, the as-synthesized SnO_2 was thoroughly observed by XRD, XPS, FESEM and HRTEM analysis. The optical behavior of the synthesized material was examined by UV–visible diffuse reflectance (DR) and photoluminescence (PL) spectroscopy. The CV, EIS, and CP investigated the electrochemical behavior of SnO_2 in the aqueous medium, both in the dark and under illumination, whereas the valence and conduction band edges were extracted from the Mott-Schottky analysis. The as-synthesized powder was subjected to the actual photocatalytic experiments for the removal of TCP in the exposure of natural sunlight. The experimental results from HPLC, TOC, and IC were linked to propose the mechanism of the degradation process.

2. Experimental details

The SnO_2 was synthesized by a facile hydrothermal route using $SnCl_4$ as a precursor. In a typical synthesis of SnO_2, an appropriate amount of $SnCl_4 \cdot 5H_2O$ (98+%, ACROS organics™) was dissolved in 100 ml of deionized water and added 0.01 g of Triton-X as a surfactant. The metallic ion solution was stirred at 80 °C for 30 min with the dropwise addition of 0.2 M ammonia solution simultaneously till the formation of the white suspension. The resultant suspension was transferred to 200 ml of Teflon-lined stainless-steel autoclave for hydrothermal treatment at 125 °C for 24 h. After cooling to room temperature, the precipitates were centrifuged, filtered and washed with deionized water and finally with 50:50 ethanol-acetone mixture to remove the surfactant and unreacted NH_4OH solution. The filtered precipitates were dried at 60 °C for 24 h. Finally, the dried powder was calcined in a muffle furnace at 400 °C for 4 h at a heating and cooling rate of 10 °C min^{-1}.

The crystal morphology of the as-synthesized SnO_2 was investigated by acquiring the XRD patterns using a Xpert x-ray powder diffractometer (Philips PW1398) with Cu $K\alpha$ radiation source from 10° to 90° (2θ) with a step of 0.05°. Applying Scherer's equation, on the intense reflections, calculated the average crystallite size of the as-synthesized material. X-ray Photoelectron Spectrometer (PHI

5000 VersaProbe II, ULVAC-PHI Inc.) investigated the probable prevalence of the Sn^{2+} states in the binding energy range of 0 eV–1100 eV. The high-resolution core level peaks were fitted to extract the binding energies. The Field Emission Scanning Electron Microscope (FEI, Quanta FEG 450, Quorum Q150R ES), Quorum technologies coupled with EDX was employed for investigation of the bulk morphology whereas High-Resolution Transmission Electron Microscope (JEM-2100 JEOL, USA) performed the fine microstructure analysis and inter-atomic spaces of the as-synthesized powder. The optical behavior of the as-synthesized powder was investigated by a Perkin Elmer UV–visible diffuse reflectance (DR) spectrophotometer (Lambda 650) in the wavelength range of 200–900 nm. The direct and indirect band gaps of the material were evaluated by applying a Kubelka-Munk transformation on the reflectance data. The evaluated band gaps were validated by Fluorescence spectro-fluorophotometer, FS-2, Sinco, Korea, at an excitation wavelength of 250 nm and recording the emission in 250 nm–850 nm range. The acquired spectra were deconvoluted and fitted for accuracy.

The charge transport in the dark and under illumination in the synthesized material was evaluated by electrochemical impedance spectroscopy (EIS), whereas the Mott-Schottky analysis was performed to evaluate the flat band potential and to specify the semiconducting nature. The stability of the material was assessed by cyclic voltammetry (CV) analysis in positive and negative potential range. For electrochemical measurements, a VSP multi-channel potentiostat (Bio-logic Science Instrument, USA) equipped with glassy carbon (GC), platinum and Ag/AgCl saturated electrodes as working, counter and reference electrodes, respectively. For the modification of GCE (working electrode), a sonicated dispersion of catalyst in chloroform was coated at the surface. The fitting of EIS Nyquist plots was performed by Zfit (Ec-lab software, Bio-logic Science Instruments, USA). A 50-W halogen lamp was used as a source for the measurements under illumination.

To evaluate the adsorption of the 2,4,6-TCP substrate on as-synthesized SnO_2 and to attain the adsorption-desorption equilibrium, a 200 cm^3 of the catalyst/TCP suspension containing 50 ppm of the substrate and optimized amount of 100 mg photocatalyst was kept in the dark for 1 h prior to exposure. For photocatalytic experiments, the suspension was exposed to sunlight (900–1100 × 10^2 lx) in a Pyrex® glass reactor (120 × 30 mm) in the fixed period of daylight from 9 a.m. to 3 p.m. Samples were drawn at regular intervals and analyzed by HPLC (SPD-20A, Shimadzu Corporation, Japan) after removing the catalyst using a 0.22 μm syringe filter. The same sample was subjected to total organic carbon (TOC) measurements using TOC-V$_{CPH}$ total carbon analyzer supplied by Shimadzu Corporation, Japan. The released chloride ions during the course of reaction were monitored by Thermo scientific, USA, ion chromatograph, Dionex (ICS-5000 + EG Eluent Generator) during the degradation/mineralization process.

3. Results and discussion

The powder x-ray diffraction profile of the as-synthesized SnO_2 in the 2θ range of 10°–90° is presented in Fig. 1a. The sharpness of the diffraction peaks reflected the high crystallinity of the synthesized material and the pattern appeared as the combination of reflections of various intensities. The major reflections at the 2θ values of ~26.65°, ~33.94°, ~38.01°, ~54.81° and ~57.86° were matched with the JCPDS# 41-1445 representing the tetragonal SnO_2 and assigned to (1 1 0), (1 0 1), (2 0 0), (2 1 1) and (0 0 2) indices of the lattice. The perceived reflections were in sound agreement with that reported in the literature for similar material synthesized by alternative routes (Sun et al., 2011). Additionally, the absence of the reflections due to the other oxides of Sn such as SnO
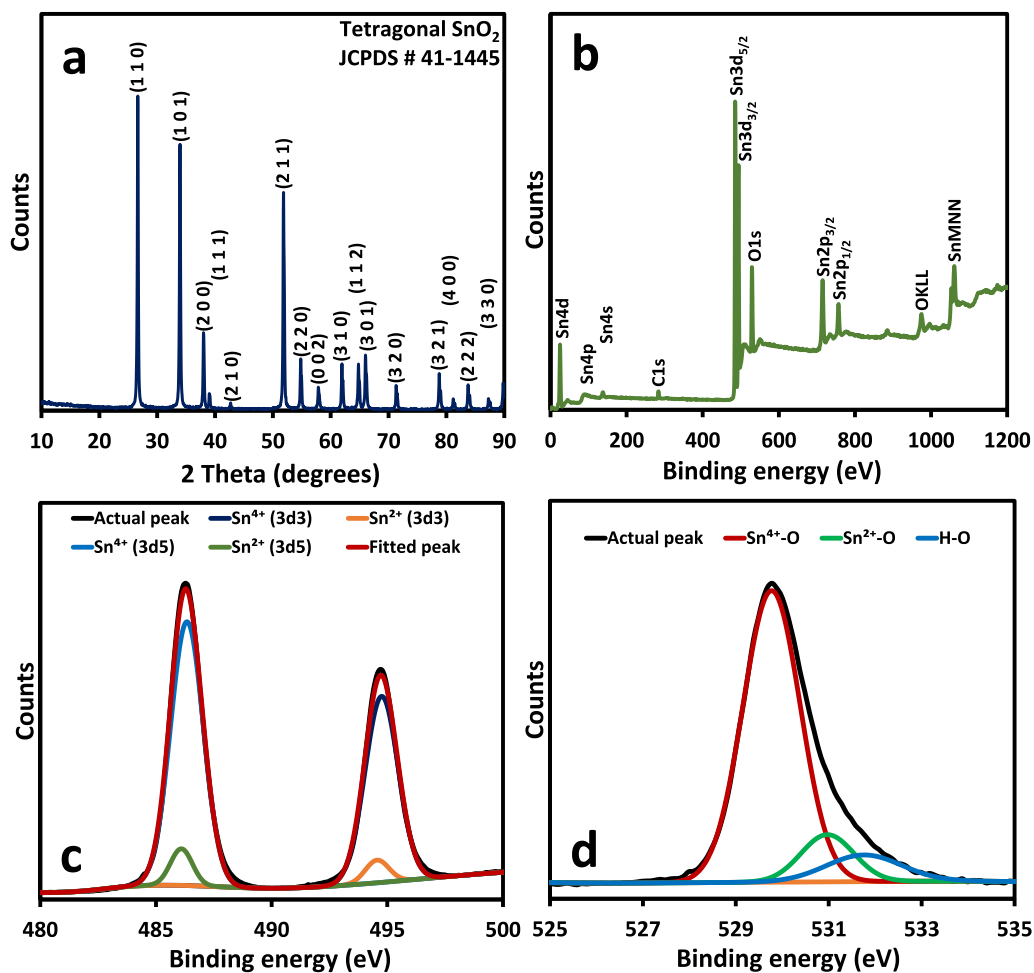
Fig. 1. (a) The XRD pattern in a 2θ range of 10°−90° (b) the XPS survey scan in the binding energy range of 0−1200 eV. The deconvoluted fitted spectra of Sn3d core level (c and d) after depth profiling.

and Sn$_3$O$_4$ substantiated the phase purity of the synthesized powder. The crystallite dimensions of the material, as evaluated by smearing the Scherer's equation on the intense reflections, revealed an average crystallite size of 41.3 nm. The chemical environment of each component and the expected probable existence of the Sn^{2+} based defects in the synthesized powder was investigated by XPS analysis. Fig. 1b shows the wide-angle survey scan of the synthesized material in a broad binding energy range of 0 eV−1200 eV, where the peaks due to essential components of the powder i.e. Sn and O are observable. The binding energy of the C1s core levels that appeared at ~283.98 eV in the current analysis was used for the correction of binding energies. As observed from the survey scan, the spin-orbit coupling resulted in the splitting of the Sn3d core level peak in a doublet with the binding energies of ~494.5 eV and ~486.2 eV whereas the O1s peak appeared at ~529.85 eV. The structural defects analysis and the probable existence of variable oxidation states of Sn was carried out by the deconvolution and the fitting of the Sn3d split core level peaks. The deconvolution of both the peaks i.e. Sn3d$_{3/2}$ and Sn3d$_{5/2}$, as presented in Fig. 1c, revealed the minor fraction of Sn^{2+} besides the abundant Sn^{4+} states. The fitting of the Sn3d$_{3/2}$ split level revealed the 2 + and 4 + states at the binding energies of ~494.72 eV and ~494.52 eV whereas, for Sn3d$_{5/2}$ levels, the same appeared at ~486.11 eV and ~486.24 eV respectively. The low intensities of Sn^{2+} peaks in both i.e. ≤ 5% of that of Sn^{4+}, exposed the overall stoichiometric nature of the

synthesized material with minor defects. The asymmetric O1s peak also indicated the variant environment of oxygen in the lattice. The deconvolution (Fig. 1d) revealed the expected intense peak of the Sn^{4+}−O bond at ~529.81 eV whereas the low-intensity peaks at ~531.06 eV and ~531.94 eV represented the oxygen attached to Sn^{2+} entities (defects) and the surface water molecules. The findings and observed binding energy values were in close agreement with the previous studies (Gubbala et al., 2009; Kar et al., 2009; Thiel, 1987).

The evaluation of the morphology of the synthesized SnO$_2$ at various magnifications (Fig. 2) revealed the fibrous clusters of the material with porous nature at the lower magnification. At higher magnification, the fibers appeared as the particles of varying shapes and sizes. The EDS analysis (inset of Fig. 2b) revealed the contributions from all the components of the sample mounted for the analysis on the grid that included C (grid material), Au (coating material), Sn and O. The elemental composition retrieved from the analysis was 69.92 wt% Sn, 25.8 wt% O and 4.4 wt% C. The calculated percentages of Sn and O, after the adjustment of the contribution from C, were close to the theoretical values. As the surface charging and unprecedented mobility of the particle in the electron beam resulted in the hazy images without credible and presentable information at higher magnification, the morphology of the synthesized SnO$_2$ powder was further investigated by the transmission electron microscopy (TEM). Fig. 3a and b, present the TEM images at the scale of 50 nm and 20 nm respectively, where the tetragonal
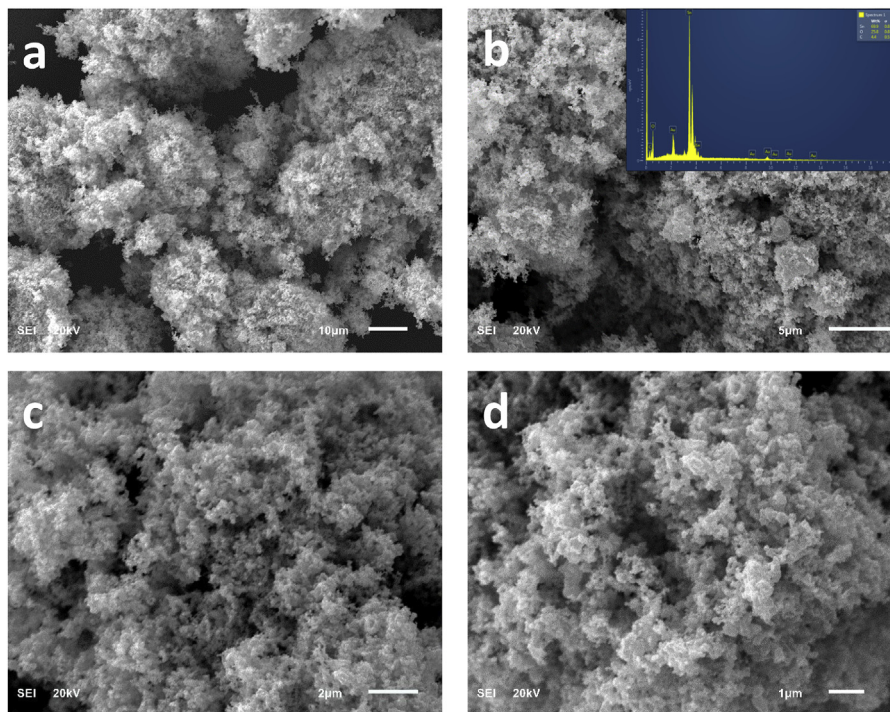
Fig. 2. The comparison of the FESEM images of as-synthesized SnO_2 at various magnifications.
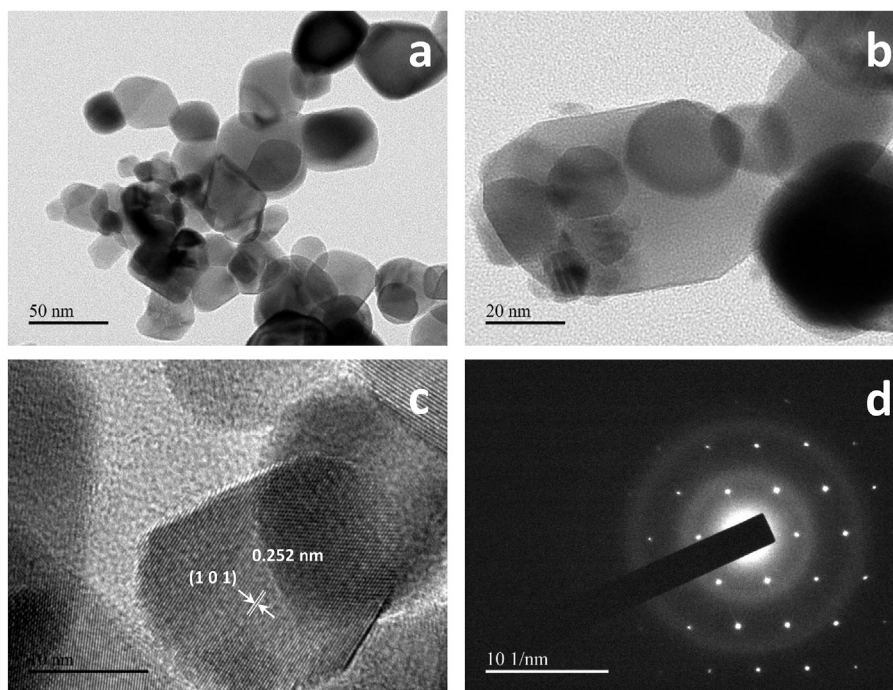

Fig. 3. The typical TEM images of SnO_2 (a and b) showing the morphology and particle size distribution. The HRTEM image (c) showing the fringe pattern of the single crystal whereas (d) shows the SAED pattern.

particles of SnO_2 with the wide particle size distribution ranging between 5 and 50 nm are observable. The focusing of the single crystal (Fig. 3c) exposed the discrete pattern of the fringes with the d-spacing of 0.252 nm that corresponded to (1 0 1) crystal planes of the tetragonal SnO_2. The isolation of the discrete atomic layer pattern also elucidated the defect-free nature of the crystal (He

et al., 2006). The SAED pattern (Fig. 3d) covered all the reflections associated with SnO_2 and validated the findings of XRD analysis.

The assessment of the optical properties that include the absorption and emission properties is an essential prerequisite for the use of the synthesized material in photocatalytic applications. The solid-state absorption spectra of the synthesized powder, recorded

in the wavelength range of 200−900 nm, is presented in Fig. 4a. A mild increase was observed in the absorbance with the decreasing wavelength that specified the presence of low energy absorbing states probably composed of Sn^{2+} based defects. On the other hand, the distinct absorption edge in 300 nm−400 nm range substantiated the well-defined band structure in the powder. Additionally, the smoothness of the spectra also indicated the assorted optimum atomic arrangement leading to high crystallinity and non-existence of the amorphous phases. In SnO_2 band structure, the 3d orbitals of Sn^{4+} states constitute the conduction band whereas the valence band is composed of O 2p entities. As the spacing between the valence and the conduction band is associated with the variations in the crystallinity and the atomic arrangement (Fan and Chu, 2014), the sharp edge in the absorption spectra refers to discrete band spacing in the material. The diffuse reflectance spectra of the powder are presented in the inset (c) of Fig. 4a, where a steep decrease in reflectance (%R) is observable in the wavelength range of 300 nm−400 nm. The %R data was subjected to Kubelka-Munk transformation to calculate (F(R)) values used in estimating the direct bandgap of the powder The graphical evaluation of the bandgap is presented in the inset (d) of Fig. 4a, where the extrapolation of the onset region of the curve to the x-axis resulted in the bandgap of the material. The estimated band energy of ~3.4 eV was in close agreement with that reported in the literature for powder (bulk) SnO_2 (Xu and Schoonen, 2000). The PL analysis (Fig. 4b),
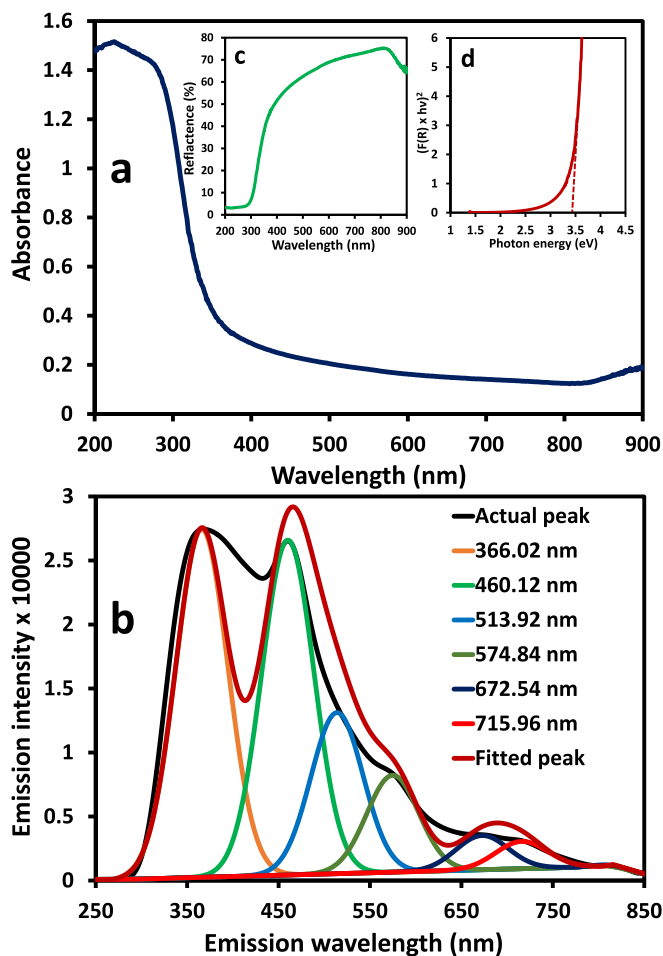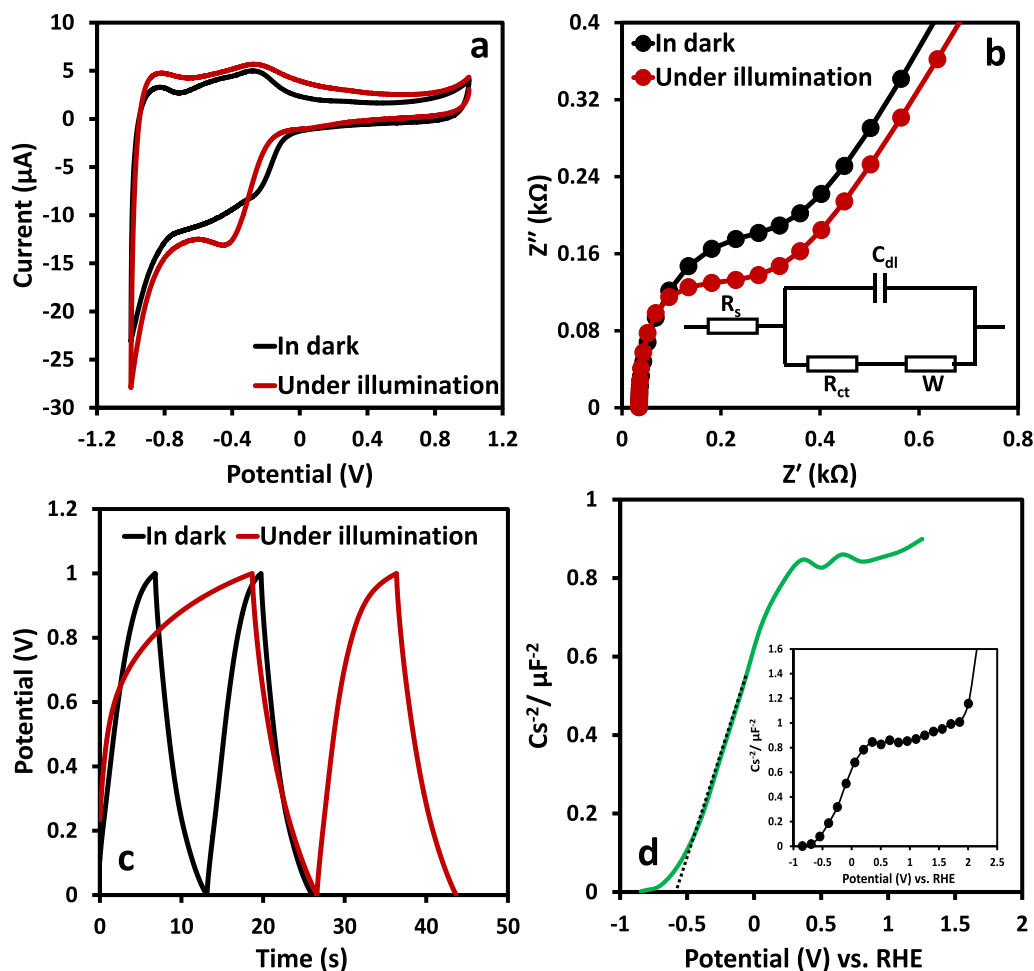
further elaborated the band structure of the material. The deconvolution and fitting of the spectra revealed the major emission bands at ~366.02 nm and ~460.12 nm. The band at ~366.02 nm equivalent to 3.38 eV photon energy represented the de-excitation from the conduction band (Sn^{4+} 3d) to the valence band (O^{2-} 2p) whereas that of ~460.12 nm (~2.69 eV) corresponded to the emission of the electrons trapped in the Sn^{2+} based defects. A similar finding was observed in the DRS analysis.

In the current investigation, the stability and the expected photocatalytic behavior of the SnO_2 under sunlight exposure were assessed by comparing the electrochemical measurements in the dark and under illumination. The CV's of the as prepared SnO_2, in the dark and under illumination, conducted in 0.1 M Na_2SO_4 solution at a scan rate of 100 mV/s and the potential range of +1.0 V to −1.0 V vs. Ag/AgCl electrode, are compared in Fig. 5a. In the dark, the pair of broad peaks at −0.30 V and −0.56 V, in the reduction curve, represented the conversion of SnO_2 into metallic Sn under the influence of the external biasing whereas a pair of sharp and broad peaks at −0.83 V and −0.31 V respectively, in the oxidation potential region, exhibited the backward process. In comparison to dark, under illumination, the reduction of SnO_2 was further enhanced with the absorption of photons and the well-shaped single reduction peak for SnO_2 into Sn was observed at −0.41 V. The CV's also revealed a better charge transfer from the SnO_2 modified electrode to the electrolyte solution or vice versa under illumination. The electrochemical impedance spectroscopy (EIS) of the SnO_2 under the identical conditions of exposure was performed in the frequency range of 100 mHz to 100 kHz with an amplitude of 10 mV at a bias of +0.23 V vs. Ag/AgCl. The comparison of the fitted Nyquist plots is presented in Fig. 5b whereas the Randle's equivalent circuit model used for the fitting is presented in the inset of the same. The R_{ct} values extracted 253 Ω and 191 Ω for the as-synthesized SnO_2 in the dark and under illumination respectively suggested the facile charge transfer behavior of SnO_2 under illumination with reduced resistance. The charge-discharge curves (Fig. 5c) depicted the prolonged discharge period of the powder, under illumination, that was in sound agreement with the EIS result (Li et al., 2013).

In aqueous phase photocatalytic processes, besides the ease of charge transport, the suitability of the potential associated with the band edges for water oxidation and reduction of adsorbed entities is of prime importance. The Mott-Schottky plot of the SnO_2 at a frequency of 1 kHz in the dark, generated from the SPEIS outcome portrayed a positive slope as expected for *n-type* semiconductor. The graphical evaluation of the onset potential of −0.60 V vs. RHE is presented in Fig. 5d whereas the original SPIES curve in the potential range of −1.0 V to 2.5 V is shown in the inset of the same. Based on the electrochemical analysis the water oxidation (+1.23 V) and the reduction of the adsorbed O_2 for the generation of reactive oxygen species (ROS) might be anticipated.

The performance of the photocatalyst for the removal (degradation/mineralization) of a contaminant in the aqueous medium is relational to its ability to generate the highly oxidizing reactive oxygen species. Although, it is well established that the hydroxyl ($HO^{\bullet}$) and superoxide anion ($O_2^{\bullet-}$) radicals are the major ROS i.e. produced in the aqueous phase photocatalytic process by water oxidation and reduction of dissolved oxygen respectively, however, their mode of generation, lifetime and mobility are still ambiguous (Pichat, 2013; Qamar et al., 2017a). Recently, some studies have raised serious objections on the generation of $HO^{\bullet}$ and proposed a complex pH dependent complex route (Pichat, 2013). In the current study, besides evaluating the suitability of SnO_2 as the potential photocatalyst for the decontamination of water, based on various experimental measurements such as the HPLC degradation pattern, estimation of released anions and TOC removal, we attempted to


Fig. 4. The solid-state absorption spectra of as-synthesized SnO_2 in the wavelength range of 200−900 nm whereas the (b) presents the fitted PL spectra at the excitation wavelength of 250 nm. The insets (c) and (d) shows the DRS and the graphical evaluation of the direct bandgap.

Fig. 5. The comparison of (a) the CV's (b) Nyquist plot of EIS and (c) the charge-discharge behavior of the synthesized SnO$_2$ in the dark and under illumination. The Mott Schottky plot for the evaluation of the flat band (V$_{fb}$) potential is presented in (d). The inset of (b) shows Randal's circuit to fit EIS data whereas the actual SPIES curve is shown in the inset of (d).

classify the contribution of each ROS in the degradation process. In addition, the generation of the above-mentioned ROS was suppressed and enhance by the $e^- $-$h^+$ scavengers and effect was assessed on the degradation process under identical conditions.

The dark experiments revealed the 12.5% decrease in the solution concentration of TCP due to adsorption that pointed the availability of the active site at the surface of SnO$_2$. The HPLC profiles for the degradation of TCP as a function of time is presented in Fig. 6a. For the pure substrate (without SnO$_2$), the HPLC peak appeared at ~13.83 min whereas the same was shifted to ~13.61 min after the addition of the catalyst. The perturbation in the ionization equilibrium because of the exchange of H$^+$ ions between the surface and the substrate is the probable cause of the shift. With the increasing exposure time, a visible decrease in the height of the peak corresponding to TCP with the successive growth of the intermediates in the retention time regions of 1–3 min and 4–6 min was evidenced. The time-scale percentage removal of TCP is presented in Fig. 6b where a ~12% decrease in the solution concentration of TCP was noticed in the initial 20 min of sunlight exposure. Approximately, ~50% of TCP was removed in 120 min of sunlight exposure whereas the complete removal (>99.5%) of the substrate was observed after 300 min of exposure. The rate of the removal of TCP was assessed by applying the Langmuir-Hinshelwood kinetic model and the plot of the ln(C$_o$/C) versus the exposure time is presented in Fig. 6b. A linear increase in the

rate of removal with the rate constant of 0.0069 min^{-1} (R^2 = 0.997) was witnessed in the initial 120 min of exposure whereas a significant deviation from the kinetic model was noticed afterward. The increased ROS to substrate ratio with the decreasing concentration is the most probable cause for the escalated rate of removal of TCP and the deviation from the kinetic model.

As the electrical nature of the principal ROS perceived to be involved in the degradation process i.e. hydroxyl (HO$^•$) and superoxide anion (O$_2^{•-}$) radical is dissimilar, therefore, a divergent mode of interaction of each with the substrate may be anticipated. It can also be presumed that the interaction of hydroxyl radicals, being neutral in nature, may lead to ample radical entities whereas that of superoxide anion (O$_2^{•-}$) radicals being negatively charged may result in the formation of abundant anionic species in the medium. To verify the same, the time-scale IC profiling of released anions in the exposed solution was carried out and presented in Fig. 6c. The increase in the concentration of chloride ions, consistent with the removal of TCP, was noticed that depicted the strong relationship between the degradation of TCP and the released Cl$^-$ ions. The release of Cl$^-$ ions in the substantial quantity, being negatively charged in nature, is only possible with the direct interaction of negatively charged rather than neutral ROS. Additionally, the attempt to identify the intermediates by the GC-MS analysis revealed a significantly lower concentration of hydroxyl groups substituted aromatic intermediates that indicated the minor
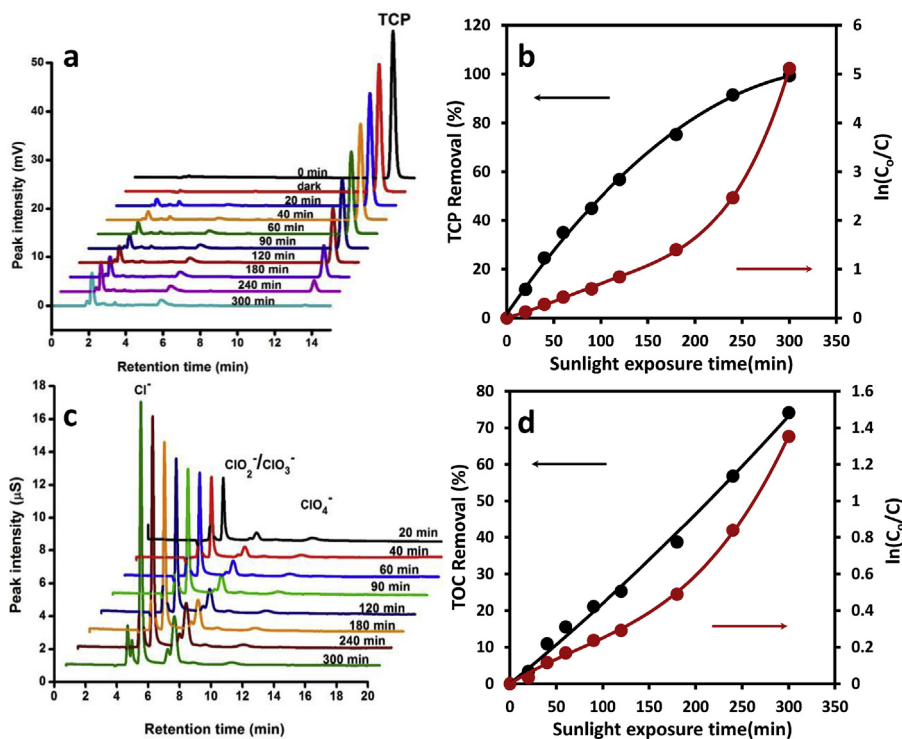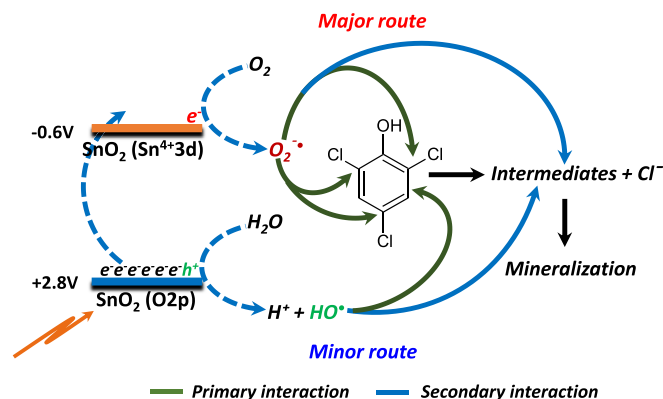
Fig. 6. (a) The time-scale HPLC profile (b) the percentage and rate of degradation (c) the IC profile for the released Cl^- ions and (d) the percentage and rate of TOC removal of 2,4,6-TCP over SnO_2 in natural sunlight exposure.

involvement of $HO^\bullet$ radicals in the degradation process. As the flat band region and the conduction band potential in the *n-type* semiconductors are end-to-end to each other (Bott, 1998), therefore the evaluated flat band potential of -0.60 V (Fig. 5d) might be regarded as the potential of the conduction band. Based on the evaluated band gap of ~3.4 eV, the valence band of the SnO_2 appeared at $+2.8$ V. Although, the evaluated valence and conduction band potentials professed the capacity of SnO_2 for the generation both hydroxyl ($HO^\bullet$) and superoxide anion ($O_2^{\bullet-}$) radicals. However, the significantly lower potential of the conduction band, the pH_{zpc} (~4.3) (Xu and Schoonen, 2000), the pH (~5.3) of the catalyst/TCP suspension, the rapid disappearance of TCP with the significantly high release of Cl^- ions and the aerated experimental condition supports the majority contribution of superoxide anion radicals. Additionally, the prolonged lifetime and the established mobility/diffusion further augment the leading role of $O_2^{\bullet-}$ as compared to $HO^\bullet$ radicals (Kwon and Yoon, 2009; Kwon et al., 2012). The time scale TOC removal during the degradation process is presented in Fig. 6d, where as compared to >99.5% removal of TCP in the 300 min of sunlight exposure, a ~75% mineralization was noticed. The comparison of the degradation and mineralization patterns revealed the simultaneous occurring of both the process, however; the lower rate of the mineralization predicted the priority of the ROS for the substrate as compared to the intermediates. The rate of mineralization (Fig. 6d) was significantly enhanced with the decreasing concentration of TCP in the solution. The same may be pictorially represented as below (see Scheme 1).

Metal ions (M^{n+}) are the documented electron capture agents in the photocatalytic processes for extending the life span of the excited states (Subramanian et al., 2003). In the current study, the effect of the various metal ions i.e. Fe^{3+}, Cu^{2+}, Ni^{2+}, and Zn^{2+} on the removal of TCP was assessed by keeping all the other experimental conditions same except for the addition of 50 ppm solution of the respective ions. The comparison of the percentage degradation of

TCP in the presence of metal ions is presented in Fig. 7a. As compared to pristine SnO_2, a significant decrease in the percentage degradation of TCP was witnessed with Cu^{2+}, Ni^{2+}, and Zn^{2+} whereas the degradation was noticeably enhanced in the presence of Fe^{3+} ions. The decreased degradation of TCP in the presence of Cu^{2+}, Ni^{2+} and Zn^{2+} clearly demonstrated the ability of the metal ions for the capture of excited conduction band electron in competition with O_2 that significantly affected the generation of $O_2^{\bullet-}$ radicals thus affecting the degradation process drastically. The observation also supported the presumption of $O_2^{\bullet-}$ radicals as majority oxidants. The enhanced degradation of TCP in the presence of Fe^{3+} ion should not be correlated with its inability to capture the excited electrons as a series of events is initiated the reaction suspension due to the exposure of Fe^{3+} ions besides the excitation of the photocatalysts itself.

Scheme 1. The plausible mechanism for the photocatalytic degradation/mineralization of TCP.
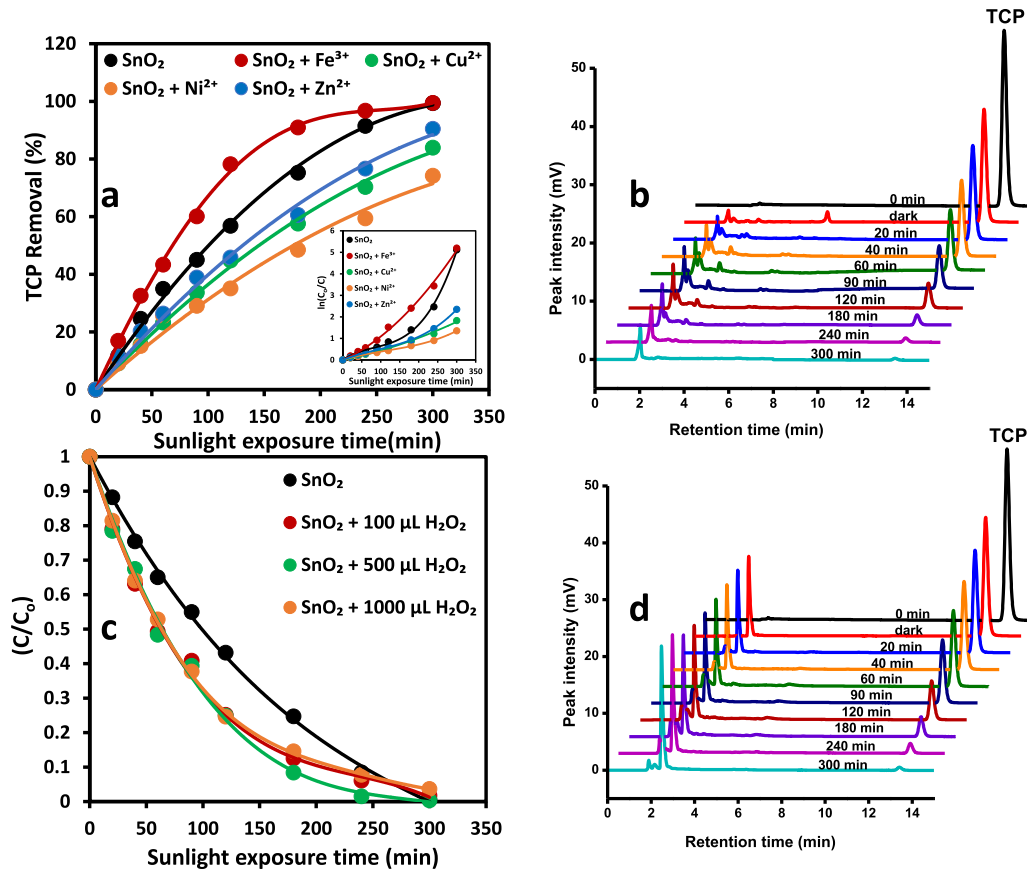
Fig. 7. (a) The percentage removal in the presence of ions (b) The time-scale HPLC profile showing the effect of Fe^{3+} ions (c) the C/C_o plots for the removal of TCP over SnO_2 in sunlight exposure (d) The time-scale HPLC profile showing the effect of 500 μL H_2O_2. The inset of (a) present the comparison of the rate of TCP removal in the presence of metal ions.

The probable major events that may occur in the suspension include:

a. The absorption of photons by SnO_2 and generation of excitons.
b. Capture of excited conduction band electrons by the Fe^{3+} to form divalent entities.
c. The initiation of photo-Fenton type reaction of the enhanced generation of ROS (Ruppert et al., 1993).
d. Initiation of fenton type reactions by the divalent Fe^{2+} (Ruppert et al., 1993).
e. Interaction of Fe^{2+} with the photo-generated holes to regenerate Fe^{3+}.
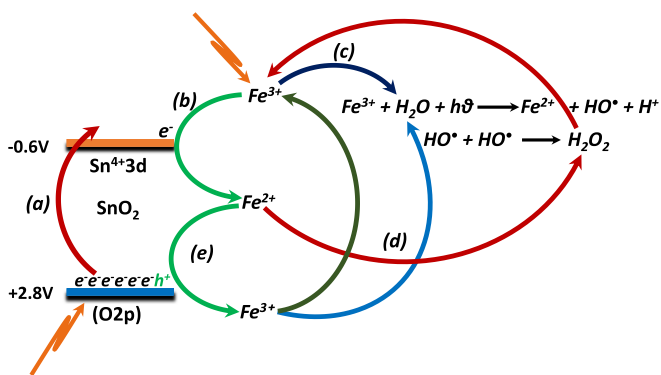
Scheme 2. An account of the probable events occurring in the medium.

The pictorial elaboration of the above-mentioned processes is presented below in Scheme 2.

The typical HPLC profile for the removal of TCP in the presence of Fe^{3+} is presented in Fig. 7b, where besides the accelerated removal of TCP, a significant variation in the nature of the intermediates, as compared to pure SnO_2 (Fig. 6a), is observable. The escalation in the removal of TCP is probably due to the enhanced formation of $O_2^{•−}$ radicals due to photo-Fenton process. For the pure SnO_2 (Fig. 6a), the identification of the low intensity intermediate in the retention time region of 4−6 min matched with the OH substituted chlorophenol that might be the probable offshoot the minor interaction of the HO$^•$ with that of TCP. The absence of the same in the presence of Fe^{3+} not only validates the formation but also authenticate the interaction of Fe^{2+} ions with that of photo-generated holes and reduced formation of HO$^•$ radicals by water oxidation. Additionally, although the formation of hydroxyl radical is well-established fact (Faust and Zepp, 1993), however, the survival in the acidic medium is vague (Pichat, 2013).

Hydrogen peroxide (H_2O_2) is a potential source of O_2 under illumination. The probable involvement of the $O_2^{•−}$ radicals in the degradation process was further investigated by the addition of various concentrations of H_2O_2. The comparison of C_o/C curves for TCP removal in the presence of various concentrations of H_2O_2 are presented in Fig. 7c. Although, as compared to pure SnO_2, a significant increase in the rate of removal of TCP was perceived for all the tested concentrations of H_2O_2, However, 500 μL appeared as the optimum. As H_2O_2 promotes the level of O_2 in the system under illumination that is regarded as the precursor for the generation of $O_2^{•−}$ radicals, therefore, authenticate the major involvement in the

removal process. The time-scale HPLC profile for the removal of TCP in the presence of 500 μL of 35% H_2O_2 solution is presented in Fig. 7c. The absence of the intermediate in the retention time region of 4–6 min, similar to that of Fe^{3+}, further authenticated the mechanism elaborated in Scheme 2.

The efficacy of the as-synthesized SnO_2 was also examined for the removal of TCP in the mixture of potential chlorophenol pollutants such as 2-chlorophenol (2-CP), 4-chlorophenol (4-CP) and 2,4-dichlorophenol (2,4-DCP). The HPLC profile for the removal of the above-mentioned pollutants is presented in Fig. 8a, where except for 4-CP, a successive decrease in the concentration of other chlorophenols is observable. The normalized peak intensity based comparison for the removal of different components is presented in Fig. 8b demonstrated that 2-CP, 2,4-DCP, and TCP are interacted simultaneously by the ROS. For 4-CP, an initial increase followed by a successive decrease is due to the ionization of the substrate by the interaction of the ROS. The stability and the formation of the polymeric structures are the additional cause in this regard (Aslam et al., 2014b, 2015b; Qamar et al., 2017b). A slightly sluggish removal of TCP was observed as compared to single component degradation i.e. sole presence of TCP is likely due to the sharing of

the ROS. The catalyst exhibited sustained activity in the six consecutive cycles with the trivial decrease in the degradation process after the third cycle. The adsorption of the ionic product is the likely source of the mild decrease.

4. Conclusions

The study established the suitability of the SnO_2 for photocatalytic decontamination of wastewater applications in natural sunlight exposure. The catalysts exhibited substantially high activity for not only the removal of TCP but also a variety of chlorophenols. The flat band potential of the as synthesized catalyst predicted the ample formation and foremost role of superoxide anions that was validated by the evidences from a variety of experimental tools. The optical, structural, electrochemical and photocatalytic properties of SnO_2 makes it a suitable substitute for TiO_2 and ZnO and predict the further improvement in the activity after suitable skeletal and surface modifications.

References

Abbas, H., Jamil, T.S., Hammad, F., 2016. Synthesis, characterization and photocatalytic activity of nano sized undoped and Ga doped $SrTi_{0.7}Fe_{0.3}O_3$ for 2,4,6-trichlorophenol photodegradation. J. Environ. Chem. Eng. 4, 2384–2393.

Affam, A.C., Chaudhuri, M., 2013. Degradation of pesticides chlorpyrifos, cypermethrin and chlorothalonil in aqueous solution by TiO_2 photocatalysis. J. Environ. Manag. 130, 160–165.

Al-Hamdi, A.M., Sillanpää, M., Dutta, J., 2015. Photocatalytic degradation of phenol by iodine doped tin oxide nanoparticles under UV and sunlight irradiation. J. Alloys Compd. 618, 366–371.

Aslam, M., Ismail, I.M.I., Chandrasekaran, S., Hameed, A., 2014a. Morphology controlled bulk synthesis of disc-shaped WO_3 powder and evaluation of its photocatalytic activity for the degradation of phenols. J. Hazard. Mater. 276, 120–128.

Aslam, M., Ismail, I.M.I., Chandrasekaran, S., Almeelbi, T., Hameed, A., 2014b. The suitability of Ce^{3+} modified ZnO photocatalyst for the mineralization of monochlorophenol isomers in sunlight exposure. RSC Adv. 4, 49347–49359.

Aslam, M., Ismail, I.M.I., Salah, N., Chandrasekaran, S., Qamar, M.T., Hameed, A., 2015a. Evaluation of sunlight induced structural changes and their effect on the photocatalytic activity of V_2O_5 for the degradation of phenols. J. Hazard. Mater. 286, 127–135.

Aslam, M., Soomro, M.T., Ismail, I.M.I., Salah, N., Gondal, M.A., Hameed, A., 2015b. Sunlight mediated removal of chlorophenols over tungsten supported ZnO: electrochemical and photocatalytic studies. J. Environ. Chem. Eng. 3, 1901–1911.

Aslam, M., Qamar, M.T., Soomro, M.T., Ismail, I.M.I., Salah, N., Almeelbi, T., Gondal, M.A., Hameed, A., 2016. The effect of sunlight induced surface defects on the photocatalytic activity of nanosized CeO_2 for the degradation of phenol and its derivatives. Appl. Catal. B Environ. 180, 391–402.

Bott, A.W., 1998. Electrochemistry of semiconductors. Curr. Sep. 17, 87–92.

Carević, M.V., Abazović, N.D., Novaković, T.B., Pavlović, V.B., Čomor, M.I., 2016. Zirconium dioxide nanopowders with incorporated Si4+ ions as efficient photocatalyst for degradation of trichlorophenol using simulated solar light. Appl. Catal. B Environ. 195, 112–120.

Chou, S.Y., Chen, C.C., Dai, Y.M., Lin, J.H., Lee, W.W., 2016. Novel synthesis of bismuth oxyiodide/graphitic carbon nitride nanocomposites with enhanced visible-light photocatalytic activity. RSC Adv. 6, 33478–33491.

Dai, G., Yu, J., Liu, G., 2012. A new approach for photocorrosion inhibition of Ag_2CO_3 photocatalyst with highly visible-light-responsive reactivity. J. Phys. Chem. C 116, 15519–15524.

Das, S., Jayaraman, V., 2014. SnO_2: a comprehensive review on structures and gas sensors. Prog. Mater Sci. 66, 112–255.

Diallo, A., Manikandan, E., Rajendran, V., Maaza, M., 2016. Physical & enhanced photocatalytic properties of green synthesized SnO_2 nanoparticles via Aspalathus linearis. J. Alloys Compd. 681, 561–570.

Dimitrov, M., Tsoncheva, T., Shao, S., Köhn, R., 2010. Novel preparation of nanosized mesoporous SnO2 powders: physicochemical and catalytic properties. Appl. Catal. B Environ. 94, 158–165.

Fan, J., Chu, P.K., 2014. Silicon Carbide Nanostructures: Fabrication, Structure, and Properties. Springer International Publishing, Switzerland.

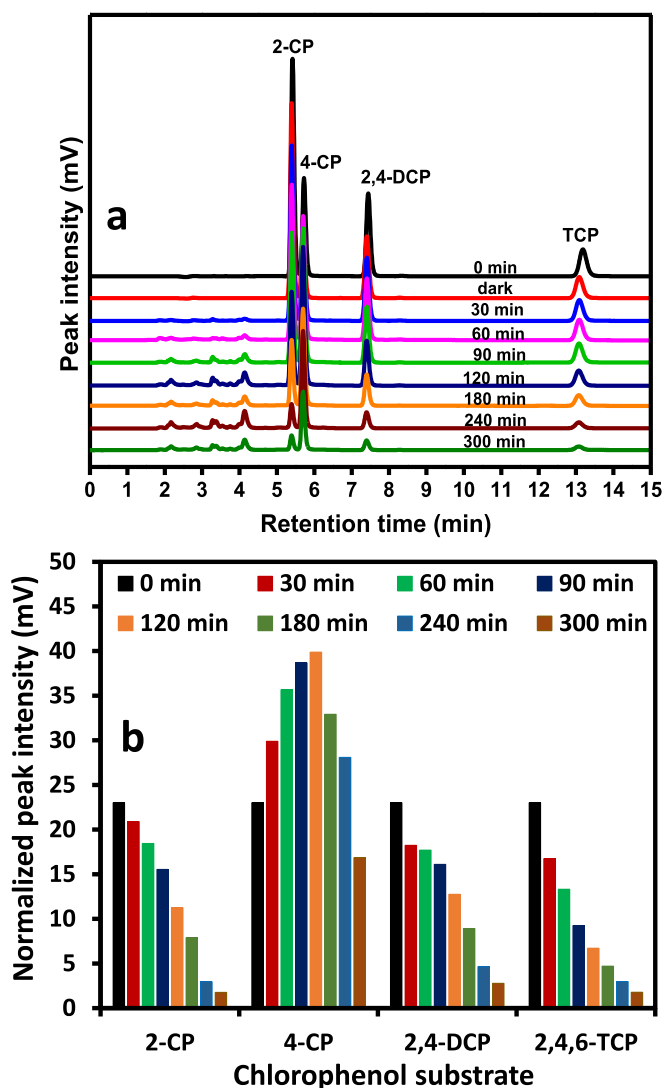Faust, B.C., Zepp, R.G., 1993. Photochemistry of aqueous iron(III)-polycarboxylate

Fig. 8. (a) The HPLC profile showing the simultaneous removal of chlorophenols (b) the peak intensity based comparison for the removal of chlorophenols over SnO_2 in sunlight exposure.

complexes: roles in the chemistry of atmospheric and surface waters. Environ. Sci. Technol. 27, 2517—2522.

Gaya, U.I., Abdullah, A.H., Hussein, M.Z., Zainal, Z., 2010. Photocatalytic removal of 2,4,6-trichlorophenol from water exploiting commercial ZnO powder. Desalination 263, 176—182.

Ghanbari, F., Moradi, M., Gohari, F., 2016. Degradation of 2,4,6-trichlorophenol in aqueous solutions using peroxymonosulfate/activated carbon/UV process via sulfate and hydroxyl radicals. J. Water Process Eng. 9, 22—28.

Gubbala, S., Russell, H.B., Shah, H., Deb, B., Jasinski, J., Rypkema, H., Sunkara, M.K., 2009. Surface properties of SnO_2 nanowires for enhanced performance with dye-sensitized solar cells. Energy Environ. Sci. 2, 1302—1309.

Hameed, A., Aslam, M., Ismail, I.M.I., Salah, N., Fornasiero, P., 2015. Sunlight induced formation of surface Bi2O4—x-Bi2O3 nanocomposite during the photocatalytic mineralization of 2-chloro and 2-nitrophenol. Appl. Catal. B Environ. 163, 444—451.

He, J.H., Wu, T.H., Hsin, C.L., Li, K.M., Chen, L.J., Chueh, Y.L., Chou, L.J., Wang, Z.L., 2006. Beaklike SnO_2 nanorods with strong photoluminescent and field-emission properties. Small 2, 116—120.

Ji, H., Chang, F., Hu, X., Qin, W., Shen, J., 2013. Photocatalytic degradation of 2,4,6-trichlorophenol over g-C3N4 under visible light irradiation. Chem. Eng. J. 218, 183—190.

Kar, A., Yang, J.Y., Dutta, M., Stroscio, M.A., Kumari, J., Meyyappan, M., 2009. Rapid thermal annealing effects on tin oxide nanowires prepared by vapor-liquid-solid technique. Nanotechnology 20, 65704.

Khaki, M.R.D., Shafeeyan, M.S., Raman, A.A.A., Daud, W.M.A.W., 2017. Application of doped photocatalysts for organic pollutant degradation - a review. J. Environ. Manag. 198, 78—94.

Kwon, B.G., Yoon, J., 2009. Experimental evidence of the mobility of hydroperoxyl/superoxide anion radicals from the illuminated TiO2 interface into the aqueous phase. Bull. Korean Chem. Soc. 30, 667—670.

Kwon, B.G., Kim, J.O., Kwon, J.K., 2012. An advanced kinetic method for HO2•/O2-• determination by using terephthalate in the aqueous solution. Environ. Eng. Res. 17, 205—210.

Li, N., Du, K., Liu, G., Xie, Y., Zhou, G., Zhu, J., Li, F., Cheng, H.M., 2013. Effects of oxygen vacancies on the electrochemical performance of tin oxide. J. Mater. Chem. A 1, 1536—1539.

Linsebigler, A.L., Lu, G., Yates, J.T., 1995. Photocatalysis on TiO2 surfaces: principles, mechanisms, and selected results. Chem. Rev. 95, 735—758.

Mendoza-Damián, G., Hernández-Gordillo, A., Tzompantzi, F., Gómez, R., 2015. Photocatalytic degradation of phenol using Al_2O_3—SnO_2 mixed oxide. J. Nanosci. Nanotechnol. 15, 7258—7261.

Nakata, K., Fujishima, A., 2012. TiO2 photocatalysis: design and applications. J. Photochem. Photobiol. C: Photochem. Rev. 13, 169—189.

Ollis, D.F., Al-Ekabi, H., 1993. Photocatalytic Purification and Treatment of Water and Air. Elsevier, Amsterdam.

Peng, H., Cui, J., Zhan, H., Zhang, X., 2015. Improved photodegradation and detoxification of 2,4,6-trichlorophenol by lanthanum doped magnetic TiO_2. Chem. Eng. J. 264, 316—321.

Pichat, P., 2013. Photocatalysis and Water Purification: from Fundamentals to Recent Applications, first ed. Wiley-VCH Verlag, GmBH Germany.

Qamar, M.T., Aslam, M., Ismail, I.M.I., Salah, N., Hameed, A., 2015. Synthesis, characterization, and sunlight mediated photocatalytic activity of CuO coated ZnO for the removal of nitrophenols. ACS Appl. Mater. Interfaces 7, 8757—8769.

Qamar, M.T., Aslam, M., Ismail, I.M.I., Salah, N., Hameed, A., 2016. The assessment of the photocatalytic activity of magnetically retrievable ZnO coated γ-Fe2O3 in sunlight exposure. Chem. Eng. J. 283, 656—667.

Qamar, M.T., Aslam, M., Rehan, Z.A., Soomro, M.T., Basahi, J.M., Ismail, I.M.I., Hameed, A., 2017a. The effect of Fe^{3+} based visible light receptive interfacial phases on the photocatalytic activity of ZnO for the removal of 2,4-dichlorophenoxy acetic acid in natural sunlight exposure. Sep. Purif. Technol. 172, 512—528.

Qamar, M.T., Aslam, M., Rehan, Z.A., Soomro, M.T., Basahi, J.M., Ismail, I.M.I., Almeelbi, T., Hameed, A., 2017b. The influence of p-type Mn_3O_4 nanostructures on the photocatalytic activity of ZnO for the removal of bromo and chlorophenol in natural sunlight exposure. Appl. Catal. B Environ. 201, 105—118.

Rengaraj, S., Li, X., 2006. Enhanced photocatalytic activity of TiO2 by doping with Ag for degradation of 2,4,6-trichlorophenol in aqueous suspension. J. Mol. Catal. A Chem. 243, 60—67.

Ruppert, G., Bauer, R., Heisler, G., 1993. The photo-Fenton reaction-an effective photochemical wastewater treatment process. J. Photochem. Photobiol. A Chem. 73, 75—78.

Salah, N., Hameed, A., Aslam, M., Babkair, S.S., Bahabri, F.S., 2016. Photocatalytic activity of V doped ZnO nanoparticles thin films for the removal of 2- chlorophenol from the aquatic environment under natural sunlight exposure. J. Environ. Manag. 177, 53—64.

Schneider, J., Matsuoka, M., Takeuchi, M., Zhang, J., Horiuchi, Y., Anpo, M., Bahnemann, D.W., 2014. Understanding TiO2 photocatalysis: mechanisms and materials. Chem. Rev. 114, 9919—9986.

Singh, L., Luwang, M.N., Srivastava, S., 2014. Luminescence and photocatalytic studies of Sm^{3+} ion doped SnO_2 nanoparticles. New J. Chem. 38, 115—121.

Sood, S., Umar, A., Mehta, S.K., Kansal, S.K., 2015. α-Bi2O3 nanorods: an efficient sunlight active photocatalyst for degradation of Rhodamine B and 2,4,6-trichlorophenol. Ceram. Int. 41, 3355—3364.

Subramanian, V., Wolf, E.E., Kamat, P.V., 2003. Influence of metal/metal ion concentration on the photocatalytic activity of TiO2-Au composite nanoparticles. Langmuir 19, 469—474.

Sun, P., Zhao, W., Cao, Y., Guan, Y., Sun, Y., Lu, G., 2011. Porous SnO_2 hierarchical nanosheets: hydrothermal preparation, growth mechanism, and gas sensing properties. CrystEngComm 13, 3718—3724.

Sun, Q., Xu, Y., 2009. Sensitization of TiO_2 with aluminum phthalocyanine: factors influencing the efficiency for chlorophenol degradation in water under visible light. J. Phys. Chem. C 113, 12387—12394.

Thiel, P.A., 1987. The interaction of water with solid surfaces: fundamental aspects. Surf. Sci. Rep. 7, 211—385.

Wang, Q., Jin, T., Hu, Z., Zhou, L., Zhou, M., 2013. TiO2-NTs/SnO2-Sb anode for efficient electrocatalytic degradation of organic pollutants: effect of TiO2-NTs architecture. Sep. Purif. Technol. 102, 180—186.

Wang, Y., Zhang, Y., Zhao, G., Tian, H., Shi, H., Zhou, T., 2012. Design of a novel Cu2O/TiO2/carbon aerogel electrode and its efficient electrosorption-assisted visible light photocatalytic degradation of 2,4,6-trichlorophenol. ACS Appl. Mater. Interfaces 4, 3965—3972.

Xiong, Z., Xu, Y., Zhu, L., Zhao, J., 2005. Enhanced photodegradation of 2,4,6-trichlorophenol over palladium phthalocyaninesulfonate modified organobentonite. Langmuir 21, 10602—10607.

Xu, L., Wang, J., 2015. Degradation of 2,4,6-trichlorophenol using magnetic nanoscaled Fe3O4/CeO2 composite as a heterogeneous Fenton-like catalyst. Sep. Purif. Technol. 149, 255—264.

Xu, Y., Schoonen, M.A.A., 2000. The absolute energy positions of conduction and valence bands of selected semiconducting minerals. Am. Mineral. 85, 543—556.

Yang, J., Chen, H., Gao, J., Yan, T., Zhou, F., Cui, S., Bi, W., 2016. Synthesis of Fe3O4/gC3N4 nanocomposites and their application in the photodegradation of 2,4,6-trichlorophenol under visible light. Mater. Lett. 164, 183—189.

Yao, L., Zhang, Y.C., Li, J., Chen, Y., 2014. Photocatalytic properties of SnS2/SnO2 nanocomposite prepared by thermal oxidation of SnS2 nanoparticles in air. Sep. Purif. Technol. 122, 1—5.

Yin, M., Li, Z., Kou, J., Zou, Z., 2009. Mechanism investigation of visible light-induced degradation in a heterogeneous TiO2/Eosin Y/Rhodamine B system. Environ. Sci. Technol. 43, 8361—8366.

Zhang, L.S., Wong, K.H., Yip, H.Y., Hu, C., Yu, J.C., Chan, C.Y., Wong, P.K., 2010. Effective photocatalytic disinfection of E. coli K-12 using AgBr-Ag-Bi2WO6 nanojunction system irradiated by visible light: the role of diffusing hydroxyl radicals. Environ. Sci. Technol. 44, 1392—1398.

Zhao, Y., Zhang, Y., Li, J., Chen, Y., 2014. Solvothermal synthesis of nonmetals-modified SnO_2 nanoparticles with high visible-light-activated photocatalytic activity in the reduction of aqueous Cr(VI). Sep. Purif. Technol. 129, 90—95.

Zhong, J., Li, J., Zeng, J., He, X., Huang, S., Jiang, W., Li, M., 2014. Enhanced photocatalytic activity of In2O3-decorated TiO2. Appl. Phys. A 115, 1231—1238.

Zhou, W., Liu, Y., Yang, Y., Wu, P., 2014. Band gap engineering of SnO_2 by epitaxial strain: experimental and theoretical investigations. J. Phys. Chem. C 118, 6448—6453.